Study on the adsorption performance of Ni-Mo-S nanomaterials for Congo red in azo wastewater

Bai Sun[a,b,*], Yunming Cheng[a], Fangwen Xu[a], Fei Liu[a], Jie Zhang[a], Zhuo Tang[a], Yun Wang[a], Jinyun Liu[c], Shuguang Zhu[a], Xinli Cai[a,*]

[a]*Key Laboratory of Water Pollution Control and Wastewater Resource of Anhui Province, College of Environment and Energy Engineering, Anhui Jianzhu University, Hefei 230601, China, Tel. +86-551-63828252; Fax: +86-551-63828252; emails: bsun@mail.ustc.edu.cn (B. Sun), ahcxl@163.com (X. Cai), 502283466@qq.com (Y. Cheng), 2392276291@qq.com (F. Xu), 765846857@qq.com (F. Liu), 1045441563@qq.com (J. Zhang), 1341451826@qq.com (Z. Tang), 596820989@qq.com (Y. Wang), zhushuguang@ahjzu.edu.cn (S. Zhu)*
[b]*Nanomaterials and Environmental Detection Laboratory, Hefei Institute of Physical Science, Chinese Academy of Sciences, Hefei 230031, China*
[c]*Key Laboratory of Functional Molecular Solids, Ministry of Education, College of Chemistry and Materials Science, Anhui Normal University, Wuhu 241002, China, email: jyliu@ahnu.edu.cn (J. Liu)*

ABSTRACT

In this paper, Ni-Mo-S (NMS) nanomaterial was prepared by a simple hydrothermal method and used as a new adsorbent to remove Congo red (CR) from azo dye wastewater. The crystal phase, morphology and microstructure of the samples were characterized by scanning electron microscopy, energy-dispersive X-ray spectroscopy, X-ray diffraction, Brunauer–Emmett–Teller surface area and Fourier transform infrared spectroscopy. The adsorption isotherm, kinetics and thermodynamics, as well as the influence of different Ni-Mo molar ratios and pH values on the experiment were studied. The experimental results show that NMS (Ni-Mo molar ratio 1:2) has a good adsorption capacity for CR. According to the Langmuir isotherm model, the maximum adsorption capacity was 490.20 mg/g. The adsorption kinetics is in good agreement with the pseudo-second-order model, and the adsorption equilibrium can be reached within 30 min. Moreover, the maximum removal rate of CR reaches 93.07% at pH = 7 and pH_{pzc} = 7.64 according to zeta potential. Finally, the mechanism of adsorption of CR by NMS (Ni-Mo molar ratio 1:2) was discussed.

Keywords: Ni-Mo-S; Nanomaterial; Adsorption; Dye wastewater

1. Introduction

Dyestuff is a kind of organic compound used to add color to other substances. Scientific literatures have indicated that the annual output of dyes is as high as 7×10^5 tons, and nearly 10%–15% of dyes are directly discharged into the environment without any treatment [1,2]. Dye wastewater has the characteristics of complex composition, high concentration of great changes in water quality and quantity, strong acidity and alkalinity, organic matter, high chroma, and great toxicity [3,4]. Direct release of dye wastewater into the environment will make a serious threat to ecological security and human health. On the one hand, even a small amount of dye in the water layer will hinder the light penetration, thus retarding the photosynthesis rate of phytoplankton and other aquatic plants [5], and have high or moderate toxicity, which can cause solemn damage to the living biota [6]. On the other hand, in addition to

* Corresponding author.

serious coloration and stimulation of human senses, many organic dyes and their aniline intermediates may cause cancer, deformity and mutation [5,7]. Congo red is an anionic acid and highly water-soluble diazo dye, as an indicator of pH in the laboratory and also as a histological stain for amyloid. It causes various health problems including difficulties in breathing, vomiting, diarrhea, somnolence and respiratory problems [8–10].

The common methods for purifying dye wastewater include adsorption [11], ozonation [12], photocatalysis [13], membrane separation [14], advanced oxidation [15], Fenton oxidation [16], coagulation–flocculation [17], etc. Among them, adsorption is one of the most effective methods for the purification of water polluted by dissolved substances and drugs [6,18]. It has advantages such as simple operation, high efficiency, a wide range of materials; and it has the ability to remove small and largely organic and inorganic, toxic and non-toxic molecules from the solution without producing any intermediate products or splitting molecules [19–21]. At present, the most common adsorbents are activated carbon [22,23], zeolite [24,25], polymer materials [26] and metal–organic framework [27]. Even some waste materials can be potential adsorbents [28,29], such as eggshell, papaya peel carbon [30], biochar from lychee seed [5], bottom ash and deoiled soya [8]. Gupta et al. [9] prepared a potential Guar gum/activated carbon nanocomposite as an adsorbent, explored the adsorption capacity at different temperatures that 359.27 mg/g at 293 K and the maximum adsorption capacity of 831.82 mg/g at 313 K. Mittal et al. [8] used bottom ash and deoiled soya for the removal of the colorant Congo red from wastewaters, which showed that deoiled soya (97.15%) and bottom ash (96.95%) had the good adsorptive ability for Congo red. It indicates that some waste materials are highly efficient adsorbents for the removal of dye from wastewaters.

Here, a granular Ni-Mo-S (NMS) nanocomposite was synthesized by hydrothermal method, and Congo red, which widely existed in industrial wastewater, was selected to simulate the organic azo pollutants in industrial wastewater. The adsorption isotherms and adsorption kinetics are also studied. The materials are characterized by scanning electron microscopy (SEM), X-ray diffraction (XRD), energy-dispersive X-ray spectroscopy (EDS), Brunauer–Emmett–Teller (BET) surface area and Fourier transform infrared spectroscopy (FTIR), and the influence of pH value on the experiment is studied. According to the experimental results, the adsorption mechanism of the material has been discussed.

2. Materials and methods

2.1. Reagents and instruments

The reagents used in the experiment mainly include nickel nitrate hexahydrate ($Ni(NO_3)_2·6H_2O$), sodium molybdate dihydrate ($Na_2MoO_4·2H_2O$), urea ($CO(NH_2)_2$), ammonium fluoride (NH_4F) and sodium sulfide nonahydrate ($Na_2S·9H_2O$) were purchased from Sinopharm Chemical Reagent Co., Ltd., (Shanghai, China) and used as received without further purification. Anhydrous ethanol, analytical purity, Xilong Scientific Co., Ltd., (China). Deionized water is prepared by FST-TOP-A24 super pure water

equipment by Shanghai Fushite Instrument Equipment Co., Ltd., (China).

The instruments used in the experiment mainly include TG16K-II table high-speed centrifuge, Shanghai Zhaodi Biotechnology Co., Ltd., (China). RCT basic magnetic stirrer, EKA Instrument Equipment Co., Ltd., (China). DHG-9023A air drying box, Shanghai Yiheng Scientific Instrument Co., Ltd., (China). PHB-3 digital pH meter, Shanghai San-Xin Instrument Factory, (China). PTFE reaction kettle, Shanghai Jinghong Experimental Equipment Co., Ltd., (China). FA2204N electronic balance, Shanghai Jinghai instrument Co., Ltd., (China). TU-1950 dual-beam ultraviolet-visible spectrophotometer, Beijing Puxi General Instrument Co., Ltd., (China). The XRD patterns of the adsorbents were performed on a D/MaXIIIA X-ray diffractometer (Rigaku Co., Japan). AURIGA scanning electron microscope, ZEISS Co., (Germany). AURIGA energy spectrometer, ZEISS Co., (Germany). BET surface area, Micromeritics Co., (USA). The FTIR spectra of the adsorbents before and after adsorption were recorded with a NEXUS-870 FTIR spectrometer (Thermo-Fisher Scientific in the USA).

2.2. Fabrication of adsorbent

NMS nanocomposites were synthesized by hydrothermal method with some modification [31,32]. 1 mmol $Ni(NO_3)_2·6H_2O$, 1 mmol $Na_2MoO_4·2H_2O$, 300 mg of $CO(NH_2)_2$ and 74 mg of NH_4F were dissolved in 50 mL deionized water, then 50 mL $Na_2S·9H_2O$ aqueous solution was added and stirred for 20 min. Different Ni-Mo ratios nanocomposites were prepared and then the reaction mixture was transferred to a 100 mL Teflon lined stainless steel reaction kettle. The reaction kettle was placed in a constant temperature heating box and heated at 120°C for 12 h. After heating, cool down to room temperature, centrifugally collect solids, wash them alternately with deionized water and absolute ethyl alcohol, and finally dry the collected solids in a vacuum drying oven at 60°C for 12 h. In order to study the effect of different Ni-Mo molar ratio of reactants on the preparation of materials, NMS samples with Ni-Mo molar ratio of 1:1, 2:1 and 1:2 were prepared and named NMS-1, NMS-2 and NMS-3.

2.3. Batch adsorption experiments

In this paper, a kind of refractory azo dye, namely acid dye Congo red (CR), was selected to simulate dyeing wastewater. Batch adsorption studies were obtained by adding NMS-1, NMS-2 and NMS-3 (20 mg) into 200 mL, 20 mg/L CR solution, respectively. And the whole experiment was carried out in a dark constant temperature shaking box with a room temperature of 25°C and a rotating speed of 150 rpm. After adsorption equilibrium, a certain amount of supernatant was taken and the absorbance of CR at the maximum absorption wavelength of 496 nm was measured by UV-Vis and analyzed.

3. Results and discussion

3.1. Sample characterization

Scanning electron microscope contains information about the surface morphology and composition of the

sample, and the image of the synthesized sample shows the particle size and high pore structure [33]. The morphology of NMS nanoparticles can be obtained by SEM, as shown in Fig. 1a–c, corresponding to the nanoparticles prepared by controlling the same reaction temperature and different Ni-Mo molar ratios (1:1, 2:1 and 1:2), respectively. As shown in Fig. 1a–c, SEM micrographs show that the particles are aggregated and distributed evenly, and there are fine gaps between the particles. The average particle size of the three adsorption materials is about tens of nanometers. In line with reference that Kumari et al. [34] prepared nano nickel sulfide to adsorb cationic dyes methylene blue (MB) and crystal violet (CV). The average particle sizes of adsorption materials NS-0, NS-1, NS-2, NS-3, NS-4 and NS-5 are 125, 130, 120, 97, 86 and 83 nm, respectively. Fig. 1d is an electron microscope image of NMS-3 after adsorption. From the image, it can be seen that obvious aggregates on the surface of the material, which shows that CR organic dye is adsorbed in the gaps and surfaces of adsorbent particles, indicating that the material has adsorption for CR.

In order to understand the effect of surface area and pore sizes on the adsorption of CR as a function of temperature, the BET surface area and pore size analysis were performed. Fig. 2a is the N_2 adsorption and desorption isotherm of NMS-3. The adsorption isotherm belongs to type III. When the relative pressure will reach 1, the adsorption capacity is far from saturation, which indicates that there are pores in the adsorbent. Fig. 2b shows the pore size distribution of NMS-3, obviously, their pore size distribution are mainly between 15 and 100 nm, indicating that the pore size of NMS-3 are mainly macropores and mesopores. The BET surface area of NMS-3 is 22.9780 m^2/g.
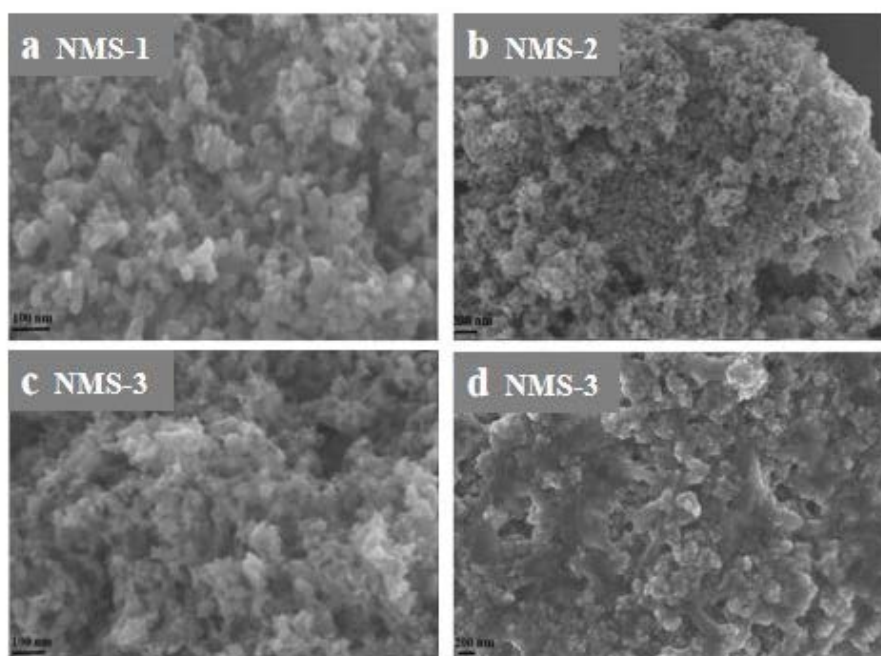

Fig. 1. SEM images of NMS nanoparticles, (a–c) before adsorption, (d) after adsorption.
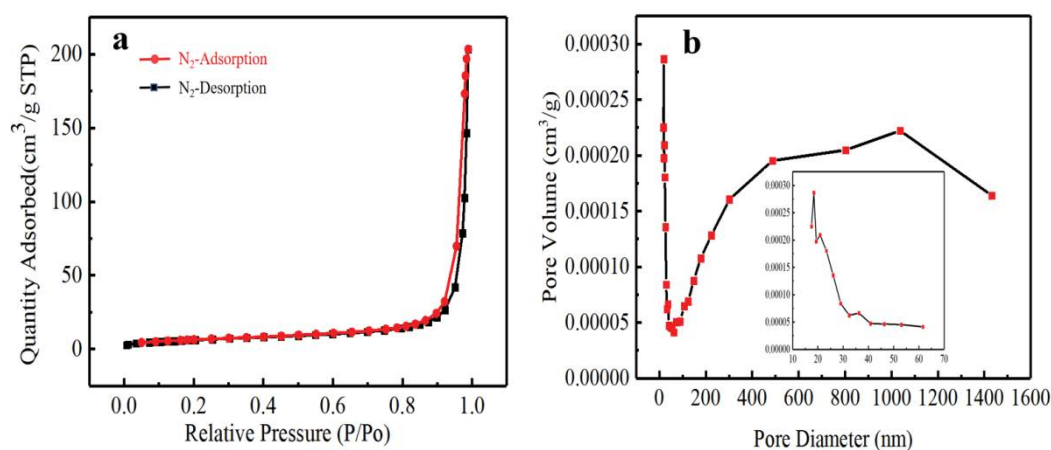

Fig. 2. (a) N_2 sorption isotherms of NMS-3 and (b) pore diameter distribution of NMS-3.

The characteristic XRD patterns of NMS-1, NMS-2 and NMS-3 adsorbents are shown in Fig. 3. The main diffraction peaks of the adsorbent are at $2\theta = 21.75°$, $31.10°$, $37.79°$, $50.11°$ and $54.61°$ respectively. It can be seen that the main diffraction peaks of the product coincide with the positions of the diffraction peaks of hexagonal crystal phase nickel sulfide (Ni_3S_2, JCPDS No. 85-1802), corresponding to (100), (–110), (111), (2–10) and (211) crystal planes, respectively. It can be seen from the figure that the positions of the main diffraction peaks in the XRD patterns of the three samples are basically consistent. The XRD diffraction peaks of NMS-3 are narrow and sharp, which indicates a high crystallinity of the adsorbent [35]. From the EDS elemental analysis (Table 1), it can be seen that the content of molybdenum in the prepared sample is very small, indicating that the molybdenum compound did not form a fixed crystal form.

3.2. Adsorptive property

20 mg sample was added into 200 mL CR organic dye with an initial concentration of 20 mg/L, and the adsorption time was 12 h. The experimental results are shown in Fig. 4. The XRD diffraction peaks of NMS-3 are narrower and higher, which indicates that the crystallinity of NMS-3 is better. Good crystallinity can ensure good structure and properties of the material [36]. It enables good surface area
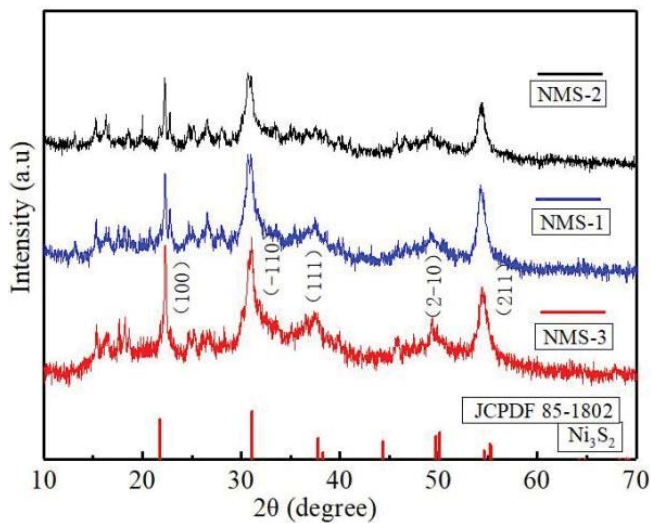

Fig. 3. XRD pattern of NMS-1, NMS-2 and NMS-3.

Table 1
Elemental composition of the synthesized NMS-3 after adsorption

Elements	Weight %	Atomic %
C K	0.36	12.74
O K	1.21	31.70
S K	2.53	33.24
Ni K	2.94	21.08
Mo L	0.28	1.24
Totals	7.32	100

and pores, few amorphous inclusions, such as residual chemicals and less crystalline defects [37,38]. According to these, NMS-3 has better adsorption capacity, which is due to the better crystallinity.

3.3. Adsorption isotherm models and thermodynamics

Freundlich and Langmuir's models were carried out to check the precise mechanism of the adsorption process and to calculate the uptake capacity [39]. In order to study the adsorption performance of NMS-3, Freundlich and Langmuir models and linear Eqs. (1) and (2) are usually used to fit the experimental results [40,41], The corresponding parameters of the two models are listed in Table 2. The thermodynamic parameters can be computed from Eqs. (3) and (4) [40].

$$\frac{C_e}{q_e} = \frac{C_e}{q_m} + \frac{1}{K_L q_m} \tag{1}$$

$$\ln q_e = \frac{1}{n}\ln C_e + \ln K_F \tag{2}$$

$$\Delta G° = -RT \ln K \tag{3}$$

$$\ln K = \frac{-\Delta H°}{RT} + \frac{\Delta S°}{R} \tag{4}$$

where C_e (mg/L) is the CR concentration after equilibrium adsorption; q_e (mg/g) is the amount of CR removed per weight of adsorbent after equilibrium; q_m (mg/g) is the maximum adsorption capacity calculated according to Langmuir equation; K_L (L/mg) is Langmuir adsorption constant; K_F (mg/g) is Freundlich adsorption constant; $1/n$ is a heterogeneous factor; R is the general gas constant (8.314 J/(mol·K)); T is the temperature (K); K is the distribution
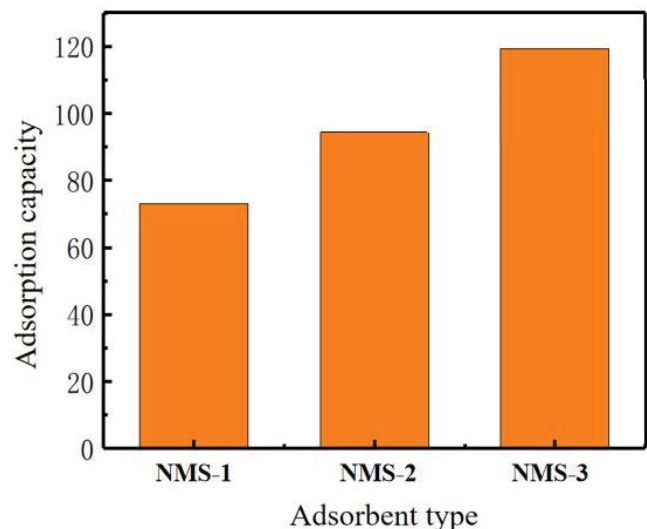

Fig. 4. Adsorption performance test of NMS nanoparticle adsorbent for CR.

coefficient of Freundlich equilibrium isotherm (L/mol); $\Delta S°$ is the entropy change; $\Delta G°$ is the change in Gibbs free energy; $\Delta H°$ is the enthalpy change.

Two isotherm models, Langmuir and Freundlich were selected to analyze the adsorption balance, and the experimental adsorption results at different temperatures fitted by the two models are shown in Fig. 5. According to Fig. 5b and c, the maximum R^2 of the Langmuir model at different temperatures is 0.9731, which is significantly smaller than the corresponding Freundlich model, indicating that the adsorption of NMS-3 on CR conforms to the Freundlich model, and the adsorption type is multilayer adsorption. According to the Langmuir isotherm

model, the maximum adsorption capacity of NMS-3 is 490.20 mg/g. Table 3 shows the comparison of the adsorption capacity of some adsorbents.

Thermodynamic analysis of adsorption is indispensable for the correct understanding and prediction of adsorption mechanism. Fig. 5a shows that at the same temperature, with the increasing of equilibrium concentration, the equilibrium adsorption capacity of CR increased. At the same equilibrium concentration, the equilibrium adsorption capacity decreased with the increasing of temperature, indicating that the adsorption performance of NMS-3 decreased with the increasing of temperature. The parameters can be calculated according to the data in Table 2, which are

Table 2
Values of various adsorption isotherm constants for the uptake of CR at different temperatures

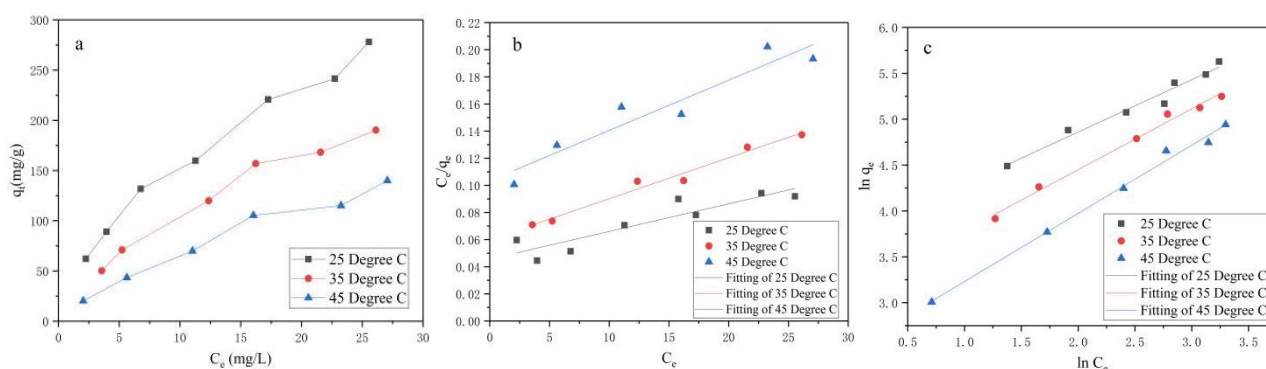| Isotherm model	Langmuir $\left(\dfrac{C_e}{q_e} = \dfrac{C_e}{q_m} + \dfrac{1}{K_L \times q_m} \right)$			Freundlich $\left(\ln q_e = \dfrac{1}{n} \ln C_e + \ln K_F \right)$		
Parameters	K_L	q_m	R^2	n	K_F	R^2
25°C	0.0446	490.20	0.8034	1.7535	24.0227	0.9630
35°C	0.0504	331.13	0.9731	1.5083	22.6463	0.9877
45°C	0.0358	270.27	0.8814	1.3469	12.0371	0.9913

Fig. 5. Adsorption thermodynamics of (a) CR at different temperatures; the fitting plot of (b) Langmuir model and (c) Freundlich model at different temperatures.

Table 3
Comparison of adsorption capacity of different adsorbents

Adsorbents	q_{max} (mg/g)	Reference
Nelumbo nucifera (lotus) leaf powder	45.89	[42]
Magnetic $Ni_{0.4}Co_{0.2}Zn_{0.4}Fe_2O_4$ nanoparticles	131.573	[43]
Graphene oxide–silica composite	333.33	[44]
Cellulose extracted from Egyptian water hyacinth	230	[45]
Chestnut husk-like nickel cobaltite hollow microspheres	366	[46]
Carbon-metal double layered oxides	317.2	[47]
Iron-zirconium mixed binary metal oxide	171	[48]
Fe_3O_4@Carbon composites	262.72	[49]
$Fe_xCo_{3-x}O_4$ nanoparticles	128.6	[50]
NMS-3	490.20	Present work

listed in Table 4. The adsorption of CR by NMS-3 is spontaneous exothermic reaction, because $\Delta G° < 0$, $\Delta H° < 0$ and $\Delta S° > 0$.

3.4. Kinetic study

Adsorption kinetics describes the adsorption rate and efficiency of dye molecules. In order to further analyze the adsorption kinetics, linear and nonlinear adsorption kinetic models were used to describe the experimental data. The nonlinear models use to decrease the errors causing from transformation of nonlinear to linear model [51]. The forms of the four models are as follows [52,53]:

Linear form of pseudo-first-order:

$$\log\left(q_e - q_t\right) = \log q_e - \frac{k_1 t}{2.303} \tag{5}$$

Linear form of pseudo-second-order:

$$\frac{t}{q_t} = \frac{1}{k_2 q_e^2} + \frac{t}{q_e} \tag{6}$$

Table 4
Adsorption thermodynamic parameters

Samples	T (K)	$\Delta G°$ (kJ mol^{-1})	$\Delta S°$ (kJ K^{-1} mol^{-1})	$\Delta H°$ (kJ mol^{-1})
NMS-3	298	–7.88		
	308	–7.99	–4.98	26.42
	318	–6.58		

Nonlinear form of pseudo-first-order:

$$q_t = q_e\left[1 - \exp\left(-k_t t\right)\right] \tag{7}$$

Nonlinear form of pseudo-second-order:

$$q_t = \frac{q_e^2 \cdot k_2 \cdot t}{k_2 \cdot q_e \cdot t + 1} \tag{8}$$

where q_e and q_t (mg/g) are the amount of CR adsorbed at equilibrium and at any time, respectively; t (min) is the adsorption time; k_1 (1/min) and k_2 (g/(mg min) are the rate constants of l inear and nonlinear models reactions, respectively.

The pseudo-first-order kinetic model is used to describe the irreversible adsorption equation of the solid–liquid system. The pseudo-second-order kinetic model is based on the assumption that chemisorption is only controlled by one or one factor. Eqs. (5) and (6) represent pseudo-first-order and pseudo-second-order dynamics models, respectively. Eqs. (7) and (8) represent nonlinear pseudo-first-order and pseudo-second-order dynamics models, respectively. As seen from Fig. 6a, the adsorption equilibrium time of NMS-3 was 30 min. The obtained theoretical equilibrium uptake capacities from the nonlinear fitting in values are close to the actual experimental value, suggesting a high accuracy. The adsorption speed of NMS-3 is relatively fast in the first 5 min, the adsorption rate decreased gradually in 5–30 min. After 30 min, the adsorption capacity of NMS-3 tended to be stable and reached the maximum, as shown in Fig. 6e and f. With the initial concentration of 5 mg/L, the linear correlation coefficient R^2 of the pseudo-second-order kinetic equation is larger than the pseudo-first-order
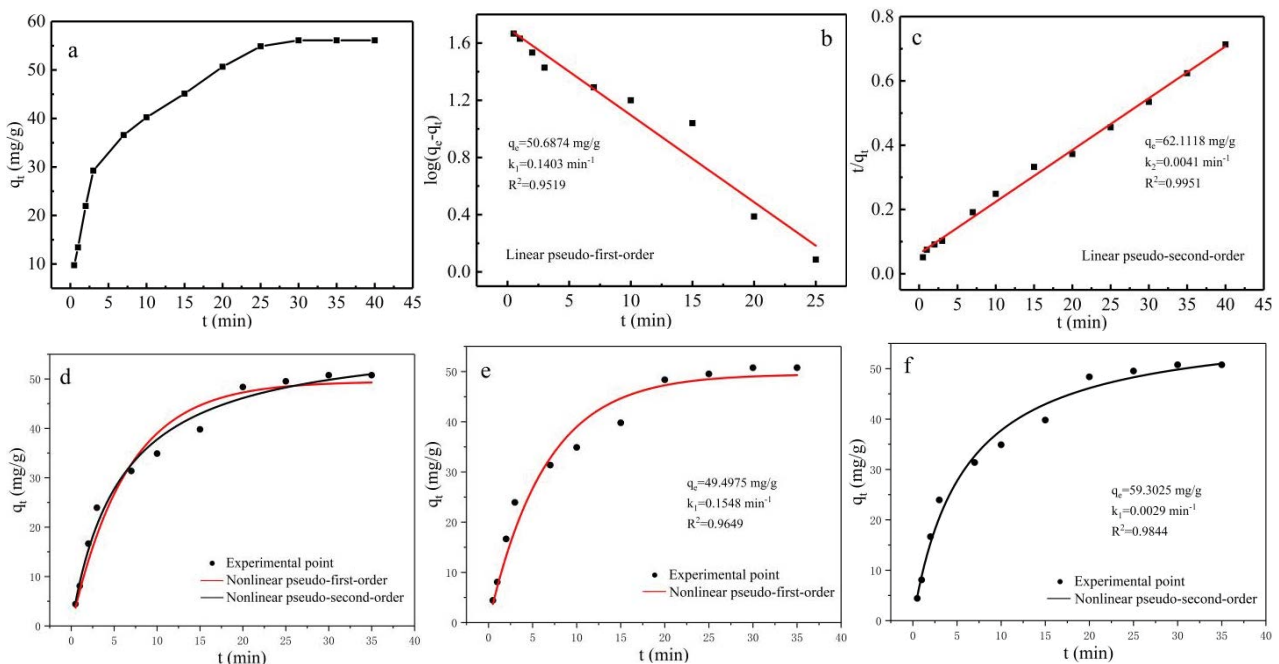

Fig. 6. (a) Adsorption capacity of NMS-3 for CR solution, (b) plot for the pseudo-first-order, (c) plot for the pseudo-second-order, (d) nonlinear pseudo-first-order and pseudo-second-order, (e) nonlinear pseudo-first-order, and (f) nonlinear pseudo-second-order.

kinetic equation, indicating that the pseudo-second-order kinetic equation is suitable for describing the kinetic process, while good fitting with the pseudo-second-order model suggests the dominance of chemisorption [54].

3.5. Effect of pH on CR adsorption

In most solid–liquid adsorption, the pH value of the solution is an important factor affecting the adsorption performance of the adsorbent. It can be seen from Fig. 7a that when $3 \leq pH \leq 7$, the removal rate of CR increased with the increase of pH. This is because the number of positive charges on the surface of NMS-3 increases. When pH = 7, the removal rate of CR is the highest, reaching 93.07%. Under alkaline conditions ($7 < pH \leq 11$), the removal rate of CR decreased with the increase of pH. This is because with the increasing of pH, –OH in the solution gradually increased, excessive negative charges appear on the surface of NMS-3, and electrostatic repulsion with CR molecules hinders adsorption, thus reducing the removal rate, in line with the conclusion by zeta potential. The zero point potential (pH_{pzc}) is 7.64, as shown in Fig. 7b. When pH < pH_{pzc}, it has positive point, and the negative charge increases when pH > pH_{pzc}.

3.6. Effect of the co-presence of competing species on CR adsorption

As the wastewater in real life is a multi-component system containing various organic and inorganic pollutants, it is very important to study the influence of NMS-3 on CR adsorption under the coexistence of competitive species. 5 mg/L CR solution with the same concentration as pH experiment was used and added 50 mL 5 mg/L methyl orange (MO, anionic dye), malachite green (MG, cationic dye) and crystal violet CV, (alkaline dye) solutions, respectively, and adjusted pH to 7. The characteristic wavelengths of several dyes are different under UV-Vis (CR = 496 nm, MO = 464 nm, MG = 617 nm, CV = 589 nm), quantification of dye adsorption by the NMS-3 was conducted with UV-Vis spectroscopy, as shown in Fig. 8. It shows that the removal rates are 64.32% (MO), 13.71% (MG), 79.23%

(CV), respectively. The removal rates are significantly reduced compared with single Congo red solution at pH = 7 (93.07%), especially when MG is mixed with CR, the removal rate of CR is only 13.71%. It indicates there is a compete adsorption among the three dyes and CR, which hinders the adsorption of NMS-3 on CR. In addition, the NMS-3 also has a certain adsorption capacity for coexisting dyes, indicating that the NMS-3 can adsorb various organic dyes and has a wide application range.

3.7. Effect of recycling of NMS-3 on adsorption

In addition to rapid adsorption and high adsorption capacity, recyclability is also important for evaluating adsorbents [55]. In this study, 0.05 mol/L NaOH [37] solution was used as an elution solution to treat the adsorbed material. In Fig. 9 the removal efficiency of CR by NMS-3 was 93.07% for the first time. After five cycles, the removal rate remained at 81.23%, indicating that the material has good recyclability.
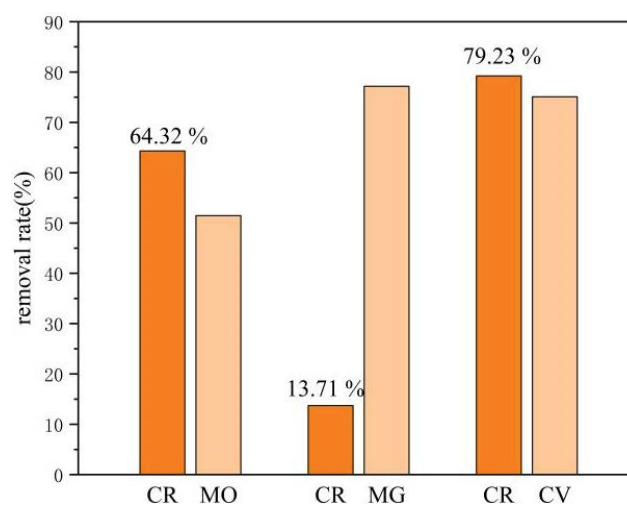

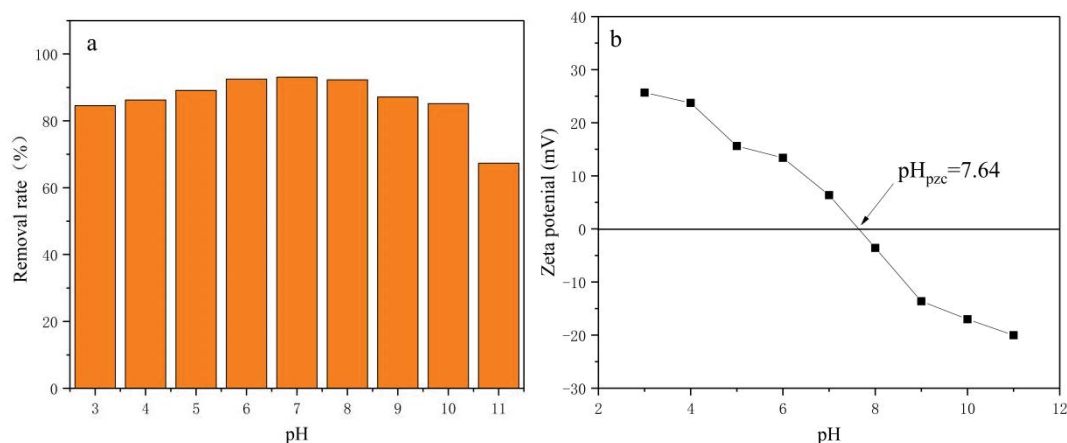Fig. 8. Effect of the co-presence of competing species on CR adsorption.

Fig. 7. (a) Effect of pH on CR adsorption and (b) zeta potential dependent on the pH of adsorbent.
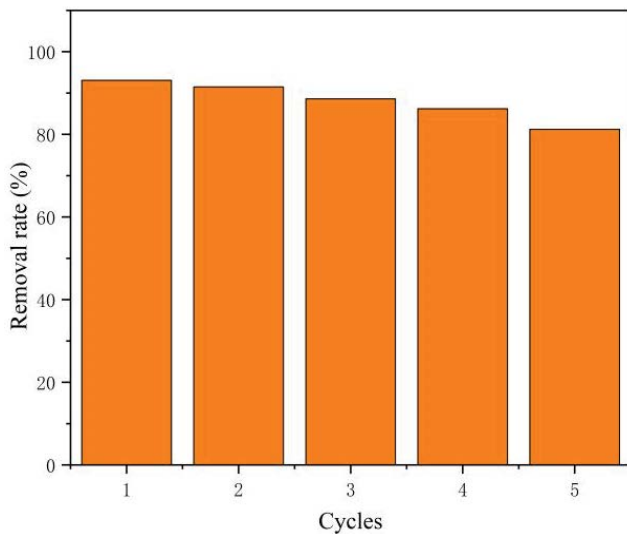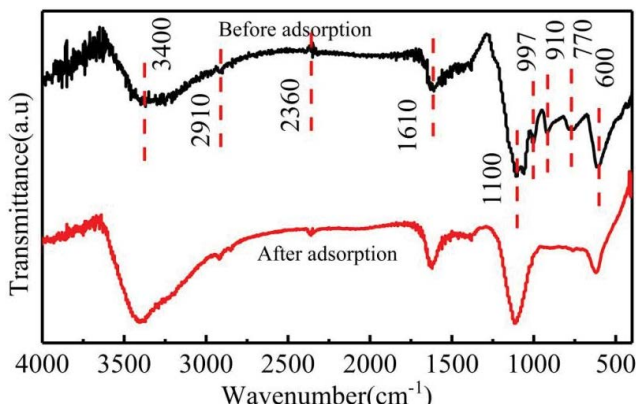
Fig. 9. Effect of recycling on CR adsorption.

Fig. 10. FTIR spectra of NMS-3 before and after adsorption.

3.8. Adsorption mechanism

The NMS-3 nanoparticle before and after adsorption were analyzed by FTIR spectroscopy, as shown in Fig. 10. The peak at 3,400 cm^{-1} becomes sharper after adsorption, which may be ascribed to the –N–H stretching vibrations in CR dye molecules and –OH bond stretching vibration in water molecules after adsorption [56]. The peak at 2,910 cm^{-1} is attributed to the stretching vibration of C–H in the alkene or aromatic groups [57,58]. The vibration peak at 2,360 cm^{-1} is due to N–H or C=O stretching vibration [59], and the peak at 1,020 cm^{-1} corresponds to N–H in-plane deformation absorption [60]. The vibration peak at 1,610 cm^{-1} is assigned to the layer surface and interlayer H$_2$O bending vibration or the C=C stretching vibration in the aromatic rings [58,61]. The main vibration band at 1,100 cm^{-1} is attributed to the stretching vibration of the S=O bond existing in the CR molecule after adsorption [56]. The new peak at 910 cm^{-1} is attributed to in-plane and out-of-plane =CH vibration [60]. Because of C-H bending vibration presence in the Congo red benzene ring, the peak at 770 cm^{-1} disappeared after adsorption [62].

The vibration peak of C-H group and sulfate (S–O bending vibration) appears at 600 cm^{-1} [63].

4. Conclusion

The NMS nanomaterial adsorbent was synthesized by a simple hydrothermal method. The adsorbent has good adsorption performance for CR. When the Ni-Mo molar ratio is 1:2, the prepared sample NMS-3 has good adsorption capacity for CR. According to the analysis of the Langmuir and Freundlich isotherm models, it can be seen that the Freundlich isotherm model is better than the Langmuir isotherm model in fitting experimental data. Langmuir isotherm model fitting shows that the maximum adsorption capacity of NMS-3 can reach 490.20 mg/g. The adsorption kinetics is in good agreement with the pseudo-second-order model, and the adsorption equilibrium can be reached within 30 min. The thermodynamics shows that the adsorption capacity of NMS-3 decreased with the increase of temperature. The pH$_{pzc}$ of the material is 7.64, and the maximum removal rate reaches as high as 93.07% at pH = 7. In addition, the adsorbent has a good recyclability, indicating a potential for application.

References

[1] T. Robinson, G. McMullan, R. Marchant, P. Nigam, Remediation of dyes in textile effluent: a critical review on current treatment technologies with a proposed alternative, Bioresour. Technol., 77 (2001) 247–255.

[2] X.M. Tian, Y.D. Song, Z.Q. Shen, Y.X. Zhou, K.J. Wang, X.G. Jin, Z.F. Han, T. Liu, A comprehensive review on toxic petrochemical wastewater pretreatment and advanced treatment, J. Cleaner Prod., 245 (2020) 118692, doi: 10.1016/j.jclepro.2019.118692.

[3] B.B. Hameed, Z.Z. Ismail, Decolorization, biodegradation and detoxification of reactive red azo dye using non-adapted immobilized mixed cells, Biochem. Eng. J., 137 (2018) 71–77.

[4] A. Mariyam, J. Mittal, F. Sakina, R.T. Baker, A.K. Sharma, Adsorption behaviour of Chrysoidine R dye on a metal/halide-free variant of ordered mesoporous carbon, Desal. Water Treat., 223 (2021) 425–433.

[5] S. Sahu, S. Pahi, S. Tripathy, S.K. Singh, A. Behera, U.K. Sahu, R.K. Patel, Adsorption of methylene blue on chemically modified lychee seed biochar: dynamic, equilibrium, and thermodynamic study, J. Mol. Liq., 315 (2020) 113743, doi: 10.1016/j.molliq.2020.113743.

[6] P. Saharan, V. Kumar, J. Mittal, V. Sharma, A.K. Sharma, Efficient ultrasonic assisted adsorption of organic pollutants employing bimetallic-carbon nanocomposites, Sep. Sci. Technol., (2021) 1–14, doi: 10.1080/01496395.2020.1866608.

[7] C. Arora, P. Kumar, S. Soni, J. Mittal, A. Mittal, B. Singh, Efficient removal of malachite green dye from aqueous solution using

Curcuma caesia based activated carbon, Desal. Water Treat., 195 (2020) 341–352.

[8] A. Mittal, J. Mittal, A. Malviya, V.K. Gupta, Adsorptive removal of hazardous anionic dye "Congo red" from wastewater using waste materials and recovery by desorption, J. Colloid Interface Sci., 340 (2009) 16–26.

[9] V.K. Gupta, S. Agarwal, R. Ahmad, A. Mirza, J. Mittal, Sequestration of toxic Congo red dye from aqueous solution using ecofriendly Guar gum/activated carbon nanocomposite, Int. J. Biol. Macromol., 158 (2020) 1310–1318.

[10] J. Mittal, Permissible synthetic food dyes in India, Reson. J. Sci. Educ., 25 (2020) 567–577.

[11] D.W. He, Q.M. Yu, Y.H. Liu, X. Liu, Y. Li, R.J. Liu, J. Xiang, Removal of Congo red by magnetic $MnFe_2O_4$ nanosheets prepared via a facile combustion process, J. Nanosci. Nanotechnol., 19 (2019) 2702–2709.

[12] Q. Zheng, Y. Dai, X.Y. Han, Decolorization of azo dye C.I. Reactive Black 5 by ozonation in aqueous solution: influencing factors, degradation products, reaction pathway and toxicity assessment, Water Sci. Technol., 73 (2016) 1500–1510.

[13] N. Bi, H.X. Zheng, Y.M. Zhu, W. Jiang, B. Liang, Visible-light-driven photocatalytic degradation of non-azo dyes over Ag_2O and its acceleration by the addition of an azo dye, J. Environ. Chem. Eng., 6 (2018) 3150–3160.

[14] C. Li, M.H. Zhang, C.W. Song, P. Tao, M.H. Sun, M.H. Shao, T.H. Wang, Enhanced treatment ability of membrane technology by integrating an electric field for dye wastewater treatment: a review, J. AOAC Int., 101 (2018) 1341–1352.

[15] S. Sundararaman, V. Kavitha, A.J. Mathew, S.M. Seby, Performance analysis of heterogenous catalyst support for the decolourisation of azo dye (Congo red) by advanced oxidation process, Biocatal. Agric. Biotechnol., 15 (2018) 384–389.

[16] N. Ertugay, F.N. Acar, Removal of COD and color from Direct Blue 71 azo dye wastewater by Fenton's oxidation: kinetic study, Arabian J. Chem., 10 (2017) 1158–1163.

[17] L. Zhou, H.J. Zhou, X.Y. Yang, Preparation and performance of a novel starch-based inorganic/organic composite coagulant for textile wastewater treatment, Sep. Purif. Technol., 210 (2019) 93–99.

[18] I. Anastopoulos, I. Pashalidis, A.G. Orfanos, I.D. Manariotis, T. Tatarchuk, L. Sellaoui, A. Bonilla-Petriciolet, A. Mittal, A. Núñez-Delgado, Removal of caffeine, nicotine and amoxicillin from (waste)waters by various adsorbents. A review, J. Environ. Manage., 261 (2020) 110236, doi: 10.1016/j.jenvman.2020.110236.

[19] S.K. Sharma, In: Hen Feather, Ed., A Remarkable Adsorbent for Dye Removal, Green Chemistry for Dyes Removal from Wastewater, Scrivener Publishing LLC, USA, 2015, pp. 409–457.

[20] A. Mariyam, J. Mittal, F. Sakina, R.T. Baker, A.K. Sharma, A. Mittal, Efficient batch and fixed-bed sequestration of a basic dye using a novel variant of ordered mesoporous carbon as adsorbent, Arabian J. Chem., 14 (2021) 103186, doi: 10.1016/j.arabjc.2021.103186.

[21] S. Soni, P.K. Bajpai, D. Bharti, J. Mittal, C. Arora, Removal of crystal violet from aqueous solution using iron based metal organic framework, Desal. Water Treat., 205 (2020) 386–399.

[22] M.B. Ahmed, J.L. Zhou, H.H. Ngo, W.S. Guo, Md. A.H. Johir, D. Belhaj, Competitive sorption affinity of sulfonamides and chloramphenicol antibiotics toward functionalized biochar for water and wastewater treatment, Bioresour. Technol., 238 (2017) 306–312.

[23] W.F. Liu, J. Zhang, C.L. Zhang, L. Ren, Sorption of norfloxacin by lotus stalk-based activated carbon and iron-doped activated alumina: mechanisms, isotherms and kinetics, Chem. Eng. J., 171 (2011) 431–438.

[24] W.A. Khanday, B.H. Hameed, Zeolite-hydroxyapatite-activated oil palm ash composite for antibiotic tetracycline adsorption, Fuel, 215 (2018) 499–505.

[25] D. Zide, O. Fatoki, O. Oputu, B. Opeolu, S. Nelana, O. Olatunji, Zeolite 'adsorption' capacities in aqueous acidic media; The role of acid choice and quantification method on ciprofloxacin removal, Microporous Mesoporous Mater., 255 (2018) 226–241.

[26] W.B. Yang, Y.Q. Lu, F.F. Zheng, X.X. Xue, N. Li, D.M. Liu, Adsorption behavior and mechanisms of norfloxacin onto

porous resins and carbon nanotube, Chem. Eng. J., 179 (2012) 112–118.

[27] S. Soni, P.K. Bajpai, J. Mittal, C. Arora, Utilisation of cobalt doped Iron based MOF for enhanced removal and recovery of methylene blue dye from waste water, J. Mol. Liq., 314 (2020) 113642, doi: 10.1016/j.molliq.2020.113642.

[28] B. Haddada, A. Mittal, J. Mittal, A. Paolone, D. Villemin, M. Debdab, G. Mimanne, A. Habibi, Z. Hamidi, M. Boumediene, E.-H. Belarbi, Synthesis and characterization of Egg shell (ES) and Egg shell with membrane (ESM) modified by ionic liquids, Chem. Data Collect., 33 (2021) 100717, doi: 10.1016/j.cdc.2021.100717.

[29] A. Patel, S. Soni, J. Mittal, A. Mittal, C. Arora, Sequestration of crystal violet from aqueous solution using ash of black turmeric rhizome, Desal. Water Treat., 220 (2021) 342–352.

[30] J. Mittal, R. Ahmad, A. Mariyam, V.K. Gupta, A. Mittal, Expeditious and enhanced sequestration of heavy metal ions from aqueous environment by papaya peel carbon: a green and low cost adsorbent, Desal. Water Treat., 210 (2021) 365–376.

[31] J. Balamurugan, C. Li, V. Aravindan, N.H. Kim, J.H. Lee, Hierarchical Ni-Mo-S and Ni-Fe-S nanosheets with ultrahigh energy density for flexible all solid-state supercapacitors, Adv. Funct. Mater., 28 (2018) 1803287, doi: 10.1002/adfm.201803287.

[32] J.W. Miao, F.X. Xiao, H.B. Yang, S.Y. Khoo, J.Z. Chen, Z.X. Fan, Y.Y. Hsu, H.M. Chen, H. Zhang, B. Liu, Hierarchical Ni-Mo-S nanosheets on carbon fiber cloth: a flexible electrode for efficient hydrogen generation in neutral electrolyte, Sci. Adv., 1 (2015) e1500259, doi: 10.1126/sciadv.1500259.

[33] N. Minju, K.V. Swaroop, K. Haribabu, V. Sivasubramanian, P.S. Kumar, Removal of fluoride from aqueous media by magnesium oxide-coated nanoparticles, Desal. Water Treat., 53 (2015) 2905–2910.

[34] S. Kumari, A.A. Khan, A. Chowdhury, A.K. Bhakta, Z. Mekhalif, S. Hussain, Efficient and highly selective adsorption of cationic dyes and removal of ciprofloxacin antibiotic by surface modified nickel sulfide nanomaterials: kinetics, isotherm and adsorption mechanism, Colloids Surf., A, 586 (2020) 124264, doi: 10.1016/j.colsurfa.2019.124264.

[35] Y. Xu, Z.P. Qu, Y.W. Ren, C. Dong, Enhancement of toluene oxidation performance over Cu–Mn composite oxides by regulating oxygen vacancy, Appl. Surf. Sci., 560 (2021) 149983, doi: 10.1016/j.apsusc.2021.149983.

[36] D.-L. Feng, Y.-Y. Zang, P. Li, Y.-H. Feng, Y.-Y. Yan, X.-X. Zhang, Polyethylene glycol phase change material embedded in a hierarchical porous carbon with superior thermal storage capacity and excellent stability, Compos. Sci. Technol., 210 (2021) 108832, doi: 10.1016/j.compscitech.2021.108832.

[37] S.N. Lin, T. Zhang, D.X. Fu, X.Y. Zhou, Utilization of magnesium resources in salt lake brine and catalytic degradation of dye wastewater by doping cobalt and nickel, Sep. Purif. Technol., 270 (2021) 118808, doi: 10.1016/j.seppur.2021.118808.

[38] S. Parashar, Q. Zhu, S. Dantas, A.V. Neimark, Monte Carlo simulations of nanopore compartmentalization yield fingerprint adsorption isotherms as a rationale for advanced structure characterization of metal−organic frameworks, ACS Appl. Nano Mater., 4 (2021) 5531–5540.

[39] S. Sahu, P. Kar, N. Bishoyi, L. Mallik, R.K. Patel, Synthesis of polypyrrole-modified layered double hydroxides for efficient removal of Cr(VI), J. Chem. Eng. Data, 64 (2019) 4357–4368.

[40] H.N. Tran, S.J. You, A. Hosseini-Bandegharaei, H.P. Chao, Mistakes and inconsistencies regarding adsorption of contaminants from aqueous solutions: a critical review, Water Res., 120 (2017) 88–116.

[41] E.C. Lima, A.A. Gomes, H.N. Tran, Comparison of the nonlinear and linear forms of the van't Hoff equation for calculation of adsorption thermodynamic parameters ($\Delta S°$ and $\Delta H°$), J. Mol. Liq., 311 (2020) 113315, doi: 10.1016/j.molliq.2020.113315.

[42] C. Meghana, B. Juhi, N. Rampal, P. Vairavel, Isotherm, kinetics, process optimization and thermodynamics studies for removal of Congo red dye from aqueous solutions using *Nelumbo nucifera* (lotus) leaf adsorbent, Desal. Water Treat., 207 (2020) 373–397.

[43] A. He, D.W. He, Z.Y. Deng, Adsorption performance of Congo red onto magnetic $Ni_{0.4}Co_{0.2}Zn_{0.4}Fe_2O_4$ nanoparticles prepared

via the rapid combustion process, J. Nanosci. Nanotechnol., 19 (2019) 5914–5920.

[44] E. Mahmoudi, S. Azizkhani, A.W. Mohammad, L.Y. Ng, A. Benamor, W.L. Ang, M. Ba-Abbad, Simultaneous removal of Congo red and cadmium(II) from aqueous solutions using graphene oxide–silica composite as a multifunctional adsorbent, J. Environ. Sci., 98 (2020) 151–160.

[45] N. Salahuddin, M.A. Abdelwahab, A. Akelah, E. Marlen, Adsorption of Congo red and crystal violet dyes onto cellulose extracted from Egyptian water hyacinth, Nat. Hazards, 105 (2020) 1375–1394.

[46] H. Chen, Y.Q. Zheng, B. Cheng, J.G. Yu, C.J. Jiang, Chestnut husk-like nickel cobaltite hollow microspheres for the adsorption of Congo red, J. Alloys Compd., 735 (2018) 1041–1051.

[47] R. Miandad, R. Kumar, M.A. Barakat, C. Basheer, A.S. Aburiazaiza, A.S. Nizami, M. Rehan, Untapped conversion of plastic waste char into carbon-metal LDOs for the adsorption of Congo red, J. Colloid Interface Sci., 511 (2018) 402–410.

[48] J. Mohanta, B. Dey, S. Dey, Highly porous iron-zirconium binary oxide for efficient removal of Congo red from water, Desal. Water Treat., 189 (2020) 227–242.

[49] L. Ren, H.X. Lin, F.C. Meng, F. Zhang, One-step solvothermal synthesis of Fe_3O_4@carbon composites and their application in removing of Cr(VI) and Congo red, Ceram. Int., 45 (2019) 9646–9652.

[50] J. Liu, N. Wang, H.L. Zhang, J. Baeyens, Adsorption of Congo red dye on $Fe_xCo_{3-x}O_4$ nanoparticles, J. Environ. Manage., 238 (2019) 473–483.

[51] S. Mallakpour, E. Khadem, Linear and nonlinear behavior of crosslinked chitosan/N-doped graphene quantum dot nanocomposite films in cadmium cation uptake, Sci. Total Environ., 690 (2019) 1245–1253.

[52] E.C. Lima, F. Sher, A. Guleria, M.R. Saeb, I. Anastopoulos, H.N. Tran, A. Hosseini-Bandegharaei, Is one performing the treatment data of adsorption kinetics correctly?, J. Environ. Chem. Eng., 9 (2021) 104813, doi: 10.1016/j.jece.2020.104813.

[53] M.I. El-Khaiary, G.F. Malash, Common data analysis errors in batch adsorption studies, Hydrometallurgy, 105 (2011) 314–320.

[54] A. Lim, J.J. Chew, L.H. Ngu, S. Ismadji, D.S. Khaerudini, J. Sunarso, Synthesis, characterization, adsorption isotherm, and kinetic study of oil palm trunk-derived activated carbon for tannin removal from aqueous solution, ACS Omega, 5 (2020) 28673–28683.

[55] C.S. Lei, M. Pi, C.J. Jiang, B. Cheng, J.G. Yu, Synthesis of hierarchical porous zinc oxide (ZnO) microspheres with highly efficient adsorption of Congo red, J. Colloid Interface Sci., 490 (2017) 242–251.

[56] S.P. Chen, R. Li, J. Qin, X.C. Guo, X.L Chen, Fabrication of novel CuO/layered double oxide microspheres and its high efficiency adsorption performance for Congo red, Colloid. Surf., A, 622 (2021) 126649, doi: 10.1016/j.colsurfa.2021.126649.

[57] H. Ouhaddouch, A. Cheikh, M.O.B. Idrissi, M. Draoui, M. Bouatia, A. Durazzo, FTIR spectroscopy applied for identification of a mineral drug substance in drug products: application to bentonite, J. Spectrosc., 2019 (2019) 2960845, doi: 10.1155/2019/2960845.

[58] B.G. Alhogbi, S. Altayeb, E.A. Bahaidarah, M.F. Zawrah, Removal of anionic and cationic dyes from wastewater using activated carbon from palm tree fiber waste, Processes, 9 (2021) 9030416, doi: 10.3390/pr9030416.

[59] Z. Filip, S. Hermann, An attempt to differentiate *Pseudomonas* spp. and other soil bacteria by FTIR spectroscopy, Eur. J. Soil Biol., 37 (2001) 137–143.

[60] S.R. Nalage, A.T. Mane, R.C. Pawar, C.S. Lee, V.B. Patil, Polypyrrole–NiO hybrid nanocomposite films: highly selective, sensitive, and reproducible NO_2 sensors, Ionics, 20 (2014) 1607–1616.

[61] X.L. Guo, Y. Ruan, Z.H. Diao, K. Shih, M.H. Su, G. Song, D.Y. Chen, S.A. Wang, L.J. Kong, Environmental-friendly preparation of Ni–Co layered double hydroxide (LDH) hierarchical nanoarrays for efficient removing uranium(VI), J. Cleaner Prod., 308 (2021) 127384, doi: 10.1016/j.jclepro.2021.127384.

[62] H. Boubaker, R.B. Arfi, K. Mougin, C. Vaulot, S. Hajjar, P. Kunneman, G. Schrodj, A. Ghorbal, New optimization approach for successive cationic and anionic dyes uptake using reed-based beads, J. Cleaner Prod., 307 (2021) 127218, doi: 10.1016/j.jclepro.2021.127218.

[63] E. Smidt, K. Meissl, The applicability of Fourier transform infrared (FTIR) spectroscopy in waste management, Waste Manage., 27 (2007) 268–276.